



# Plastic Behavior of Ferrite–Pearlite, Ferrite–Bainite and Ferrite–Martensite Steels: Experiments and Micromechanical Modelling

Saroj Kumar Basantia<sup>1,2</sup> · Ankita Bhattacharya<sup>3,4</sup> · Niloy Khutia<sup>1</sup> · Debdulal Das<sup>3</sup>

Received: 8 August 2019 / Accepted: 27 October 2019 / Published online: 9 November 2019  
© The Korean Institute of Metals and Materials 2019, corrected publication 2021

## Abstract

In this work, low carbon low alloy steel specimens were subjected to suitable heat treatment schedules to develop ferrite–pearlite (FP), ferrite–bainite (FB) and ferrite–martensite (FM) microstructures with nearly equal volume fraction of hard second phase or phase mixture. The role of pearlite, bainite and martensite on mechanical properties and flow behaviour were investigated through experiments and finite element simulations considering representative volume elements (RVE) based on real microstructures. For micromechanical simulation, dislocation based model was implemented to formulate the flow behaviour of individual phases. The optimum RVE size was identified for accurate estimation of stress–strain characteristics of all three duplex microstructures. Both experimental and simulation results established that FM structure exhibited superior strength and FP structure demonstrated better elongation while FB structure yielded moderate strength and ductility. The von Mises stress and plastic strain distribution of the individual phase was predicted at different stages of deformation and subsequent statistical analyses indicated that hard phases experienced maximum stress whereas, maximum straining occurred in soft ferrite phase for all three structures. Micromechanical simulation further revealed that strain accumulation occurred at the F–P and F–B interfaces while the same was observed within the martensite particles apart from the F–M interfaces for FM. These observations were further substantiated through the identification of void and crack initiation sites via subsurface examinations of failed tensile specimens.

**Keywords** Steel · Microstructural modelling · Representative volume element · Finite element simulation

## 1 Introduction

The global rise in need for manufacturing the fuel efficient high performance vehicles with eminent design and great comfort without conceding the safety of the passenger has led to the employment of advanced high strength steels (AHSS) in automobile industries. The attractive combinations of material properties like high strength and ductility make them the most frequently used materials worldwide [1–4]. These unique combinations of properties are achieved due to characteristics of microstructure via a controlled heat treatment process containing hard secondary phase namely pearlite, bainite or martensite dispersed in a soft ferrite matrix. Few earlier experimental investigations had revealed that the diverse range of mechanical properties can be produced by varying the microstructural parameters like grain size, volume fraction, constituent phase morphology etc. [5, 6].

In this context, several investigations were carried out earlier and the significant findings were reported as follows.

---

✉ Niloy Khutia  
niloykhutia@gmail.com; niloy@aero.iiests.ac.in

<sup>1</sup> Department of Aerospace Engineering and Applied Mechanics, Indian Institute of Engineering Science and Technology, Shibpur, Howrah, West Bengal 711103, India

<sup>2</sup> School of Mechanical Engineering, Kalinga Institute of Industrial Technology (D. U.), Bhubaneswar, Odisha 751024, India

<sup>3</sup> Department of Metallurgy and Materials Engineering, Indian Institute of Engineering Science and Technology, Shibpur, Howrah, West Bengal 711103, India

<sup>4</sup> Department of Metallurgical and Materials Engineering, Indian Institute of Technology, Kharagpur, West Bengal 721302, India

Gladman et al. [6] investigated that the ferrite grain size became smaller with the increase in its volume fraction, which eventually enhanced the yield strength (YS) and also ultimate tensile strength (UTS) of ferrite–pearlite dual phase (FPDP) structure. These investigators further stated that the interlamellar spacing of FPDP steel having higher pearlite phase volume fraction had a major influence on its mechanical behaviour. This finding was also reported by Bae et al. [7]. Additionally, Bae et al. [7] had also reported that percentage of carbon has a strong influence in determining the strength of FPDP steel. The results obtained from the experiments by Kumar et al. [8] had concluded that a significant enhancement in tensile strength and hardness occurred with an increase in the volume fraction of martensite phase. The survey carried out by Kim et al. [9] had revealed that the ductility and yield strength of ferrite–martensite dual phase (FMDP) steel was enhanced remarkably due to a presence of insignificant amount of bainite phase, however, the UTS of the material was reduced further. The study conducted by Fallahi et al. [10] on FMDP steel with 0.1% carbon content had concluded that the tensile and impact properties of this steel was affected by changing the martensite phase volume fraction ( $V_m$ ) and, the optimum properties were achieved when  $V_m$  is well within 30% to 40% [11–13].

It was observed from the previous studies that a sharp correlation exists between the microstructural variables and mechanical behaviour of duplex steels. Consequently, the duplex steel with tailored mechanical properties can be developed by controlling the microstructural parameters. In the recent past, several researchers developed the microstructure based model, or the artificial equivalent models using finite element methods to estimate the bulk mechanical properties of different materials. In this context, the finite element analysis was implemented by considering the constitutive phase properties as input parameters which were determined from the well-established numerical formulations based on the chemical composition and microstructural characteristics of the materials [14–16]. These optimisation techniques assisted in minimizing the huge cost and time consumed during the trial and error methods for the development of proper microstructure with desired mechanical properties.

In the recent past, many researchers made an attempt to predict the elasto-plastic behaviour of many AHSS from the computational analysis using virtually developed RVE models generated by mimicking the actual microstructure [17–19]. Al-Abbasi and Nemes [18] had performed the micromechanics modelling of dual phase steels using unit cell model with several idealisations. These authors had observed that the stacked hexagonal array (SHA) model with axisymmetric idealisations in which martensite particle with spherical shape was dispersed in soft ferrite phase can well capture the stress–strain behaviour of the

material considered. Ishikawa et al. [19] had considered an axisymmetric unit cell model with an assumption that the second phase particles arranged in a regular array to simulate the deformation behaviour of ferrite–pearlite steel. The estimated flow behaviour predicted from the modelling was in-line with the experiment. The effect of second phase morphology and its distribution remains an unresolved issue when using the computational study through virtual developed FE model. Further, with an objective of improving the performance of the computational model, many researchers emphasised on generating model from the real microstructures obtained experimentally [20–25]. Sun et al. [21] developed the RVE model from microscopy image of dual phase steel and performed the finite element analysis. These investigators had successfully predicted the stress–strain response, failure mode and ductility of the steel. Further Marvi-Marshhdi et al. [23] had predicted the flow behaviour of dual phase steel with 18% and 44% of hard martensite phase. These workers had performed the computational analysis on a 2D RVE model generated from scanning electron microscopy (SEM) images. The strength and ductility of the material predicted from FE simulation were closer to the experimental value.

In the present work, the authors have primarily intended to predict the stress–strain behaviour of three different duplex microstructural steels namely; ferrite–pearlite (FP), ferrite–bainite (FB) and ferrite–martensite (FM) developed with closely equal volume fractions of hard phase via a controlled heat treatment process. It was evident from the pertinent literature that incorporation of real microscopic details of phase morphologies for all three microstructures especially FP and FB in the computational model has not been explored by the previous researchers. Also, the development of the computational model to predict flow behaviour of ferrite–pearlite and ferrite–bainite microstructure was very few in the existing literature. Therefore, finite element analysis using microstructure based 2D RVE model for all three developed duplex microstructural steels (FP, FB and FM) were performed to predict their flow behaviour as well as stress–strain responses in their constituent phases in the present research. RVE models were generated through optical micrographs image analysis using image processing software, which converts the binary optical microscopic images with a particular morphology of different phases, to finite element meshed model which served as an input to the finite element software (ABAQUS). The essential parameters were obtained from the microstructural characterisation and chemical composition of the selected materials as well as from the available literature. Finite element simulations were performed with varying RVE sizes and the results of the simulations were validated by comparing the simulation responses with the experimental ones in order to find the optimum RVE size. Finally, the micromechanical modelling

and simulations were performed considering the optimum RVE size to predict the stress–strain behaviour of bulk material and also the stress–strain distributions in the constitutive phases.

## 2 Materials and Methods

Material selected for this study was a low-carbon low-alloy steel received as cold rolled bar of approximately 22 mm thick. The chemical composition of the selected material was varified by spectroscopic analysis and the acquired results are summarised in Table 1. To design the heat treatment schedule, the time–temperature–transformation (TTT) diagram of the chosen steel was first developed following the relationships proposed by Bhadeshia [26].

Initially, the round specimen blanks of 150 mm length  $\times$  16 mm diameter were machined keeping the rolling direction as longitudinal one. These specimens were subjected to three different heat treatment schedules as illustrated in Fig. 1a to develop ferrite–pearlite (FP), ferrite–bainite (FB) and ferrite–martensite (FM) microstructures. Different temperatures were selected considering the developed TTT diagram. Furthermore, several preliminary heat treatments were carried out and the developed

microstructures were characterised before finalising the heat treatment parameters in order to achieve nearly same volume fraction of second phase/phase mixture, i.e., pearlite, bainite and martensite. The details of the selected times and temperatures are mentioned in Fig. 1a.

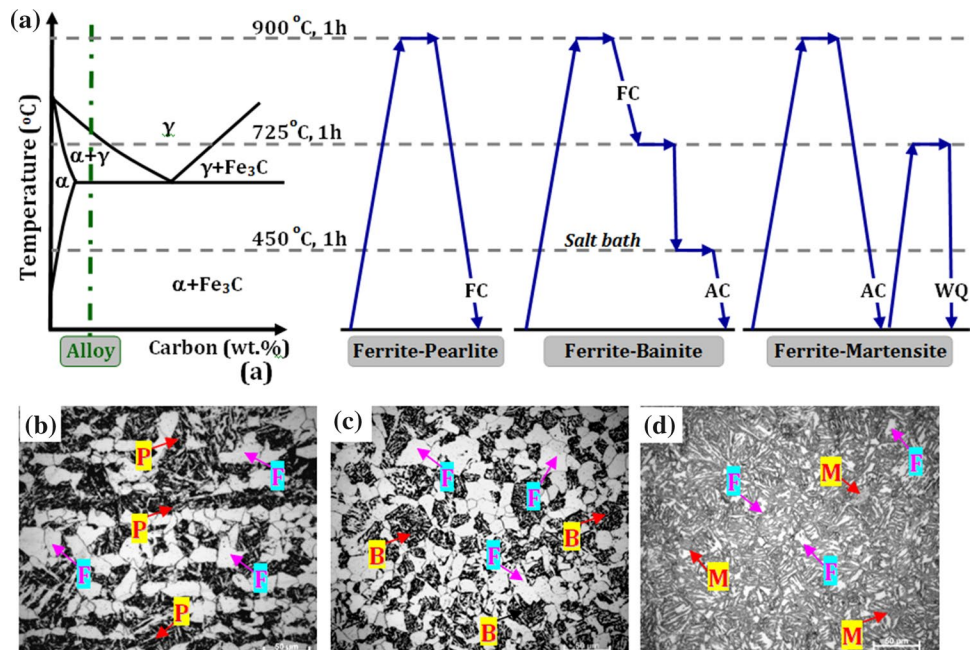
Heat treated round specimen blanks were subsequently machined to prepare tensile specimens as per ASTM E8 standard [27]. Machined round tensile samples were polished to obtained mirror finish surface. Cylindrical tensile specimen with gauge length of 32 mm and diameter of 6 mm was machined from the heat treated specimen blanks. Uniaxial tensile tests were conducted at room temperature ( $\sim 25^\circ\text{C}$ ) using a servo hydraulic controlled universal testing machine (Model: Instron 8801) with a maximum capacity of  $\pm 100$  KN. The tests were carried out at a constant strain rate of  $10^{-3} \text{ s}^{-1}$  till failure. Fractured tensile specimens and their subsurfaces were critically examined under scanning electron microscope (SEM) to identify the modes and mechanisms of failure. Subsurface specimens were prepared by WEDM machining followed by hot conductive mounting and standard metallographic polishing and etching techniques.

Grip portion of the tensile samples were used for microstructural characterisation. Specimens were mechanical polished using SiC emery papers up to grit size of 2000

**Table 1** Chemical composition of the selected steel

Element	C	Si	S	P	Mn	Ni	Cr	Mo	V	Cu	Fe
wt%	0.21	0.25	0.007	0.011	1.3	0.22	0.20	0.14	0.004	0.12	Balance

**Fig. 1** a Schematic presentation of heat treatment schedules and associated parameters employed for the development of ferrite–pearlite, ferrite–bainite and ferrite–martensite microstructures. Optical microstructures of b ferrite–pearlite, c ferrite–bainite and d ferrite–martensite steels etched using 2% Nital solution. FC: Furnace cooling; AC: Air cooling; WQ: Water quenching



followed by cloth polishing, and finally by using diamond paste up to 1  $\mu\text{m}$ . Specimen surfaces were etched for 30 s using 2% nital solution (98%  $\text{C}_2\text{H}_5\text{OH}$  + 2 vol % concentrated  $\text{HNO}_3$ ) to reveal the individual phases present within the microstructures. Optical microscope (*Model*: Carl Zeiss Axiovert 40 MAT) and SEM (*model*: JSM-7610F, JEOL Japan) were used to record the digital images at different magnifications. Axio-vision (version 3.8.2) image processing software was employed to estimate different microstructural parameters considering at least ten images for each batch of heat treated sample.

### 3 Micromechanics Based FE Modelling

Micromechanical modelling using representative volume element (RVE) model is a well-established method, which is being used to compute the macroscopic response of multi phase steels considering the microstructural parameters e.g. volume fraction, morphology, grain size etc. of its constituent phases [18]. In the present work, an RVE model has been developed considering real microstructural characteristics of the material. The size of the RVE should be large enough to incorporate all the microstructural features and on contrary the RVE should be as small as possible for optimum use of computational resources (memory and time) [28]. Many researchers have followed this method to predict the material behaviour in macro scale by giving different microstructural parameters of individual phase and found acceptable results. Different methods were used to generate the RVE model for example, unit cell RVE model, virtually developed RVE model considering different microstructural parameters and real microstructural based RVE model etc. [14, 18, 29–31].

However, very few attempts were made in order to study the effect of real microstructure in FE simulation of dual phase steel. It was noticed that the influence of grain size, morphology, interlamellar spacing etc. can be effectively addressed if the RVE model is prepared from real microstructure. In the past, Zhou et al. [31] had developed RVE model of size 110  $\mu\text{m}$  x 110  $\mu\text{m}$  taken from ten different locations of the optical images and their average stress–strain curve was compared with the experiments. But, the variation of the results with different sizes of the RVE was not considered. The effect of the RVE size on the flow behaviour of duplex steel was also investigated by Ramazani et al. [24] where the variation of yield stress was plotted in terms of RVE size as well as quantity of martensite particles. It was also observed by Cheong et al. [32] that microstructural length scale of the RVE model has significant influence on the overall response of polycrystalline materials. In the present study, size of the RVE models was varied for each of the duplex steel

microstructures where the volume fraction of the hard phase remained constant. Both YS and UTS obtained from the simulations were compared with the experiment and the optimum size of the RVE was determined for each material. In addition, the element size used to develop the RVE model was also varied to investigate the mesh sensitivity of RVE model of these composite dual phase structures and determine the optimum mesh size of the model for all three duplex microstructural steels.

#### 3.1 Generation of Finite Element Based RVE Model from Optical Microscopy Images

In the present study, the microstructure based 2D RVEs were generated from optical micrographs of FP, FB and FM steel, as shown in Fig. 1b–d. Individual phases in the microscopy images can be identified due to the variation in grey scale value. The white areas representing the ferrite phase whereas the second phases like pearlite, bainite or martensite were identified by the dark area present in the microscopy images. These microscopy images were processed subsequently through an image processing software to generate finite element models. This imaging software assigned different colours by applying proper threshold value on the optical images. It was possible to capture the morphology and volume fraction of individual phases accurately. The microstructure image captured by optical microscopy was processed through the imaging software; Simpleware with version ScanIP 2016.09-SR1. Following standard image processing steps, the microscopy images were converted into required finite element meshed model. The meshed models generated from the optical microscopy images through imaging software are displayed in Figs. 2a, 3a and 4a for FP, FB and FM structures respectively. A wide range of RVE meshed models of varying dimensions were developed for determining the optimum RVE size which can predict the macroscopic behaviour of the considered materials. The commercial finite element package ABAQUS-6.14 FE solver was used to perform the finite element analysis. The microscopic model was meshed with continuum plane strain four noded reduced integration elements (CPE4R) [14, 33]. Y-symmetry and X-symmetry boundary conditions were applied along all the nodes of the bottom edge and right-hand edge of the RVE model. The FE simulation for uniaxial tensile test was performed in displacement control model. The boundary conditions were applied according to Zhou et al. [31]. Uniform displacement was applied on the nodes of the left hand side edge of the RVE model under displacement-controlled loading. The material properties of the constituent phases were estimated through dislocation based

**Fig. 2** **a** Selection of micro-structure based 2D RVE models from optical image of ferrite–pearlite (FP) microstructure. **b** Effect of simulated stress–strain behaviour with variation in 2D RVE size. **c** Comparison of experimental yield strength as well as ultimate tensile strength with simulated results for varying RVE size

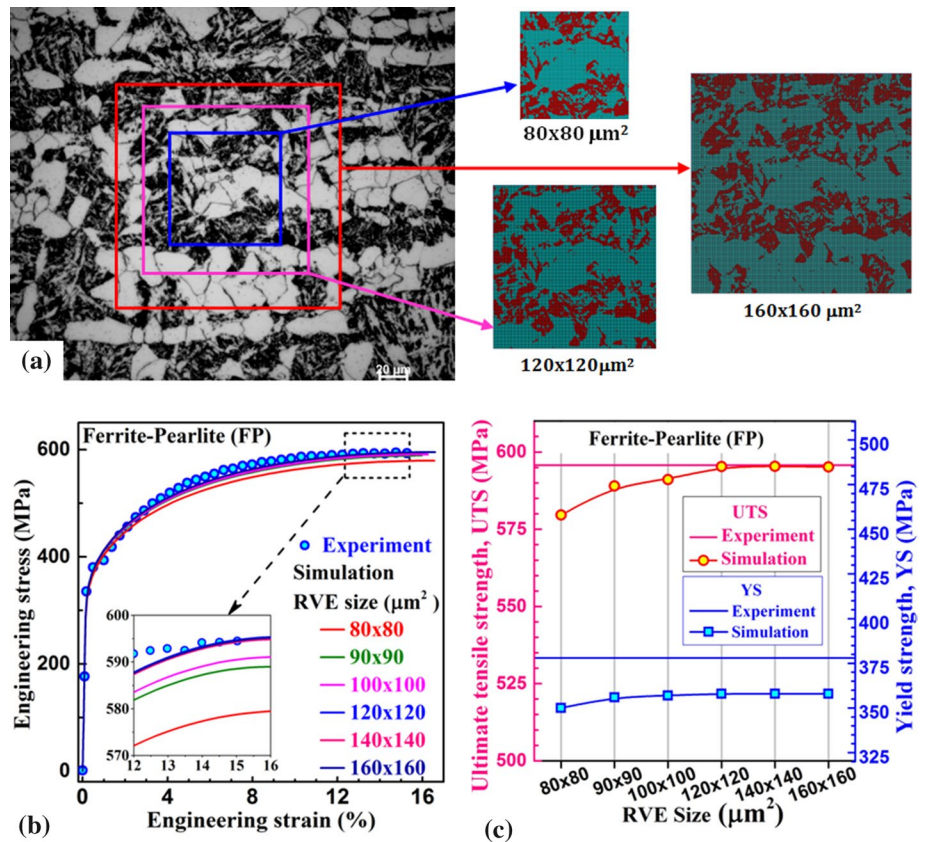


**Fig. 3** **a** Selection of micro-structure based 2D RVE models from optical image of ferrite–bainite (FB) microstructure. **b** Effect of simulated stress–strain behaviour with variation in 2D RVE size. **c** Comparison of experimental yield strength as well as ultimate tensile strength with simulated results for varying RVE size

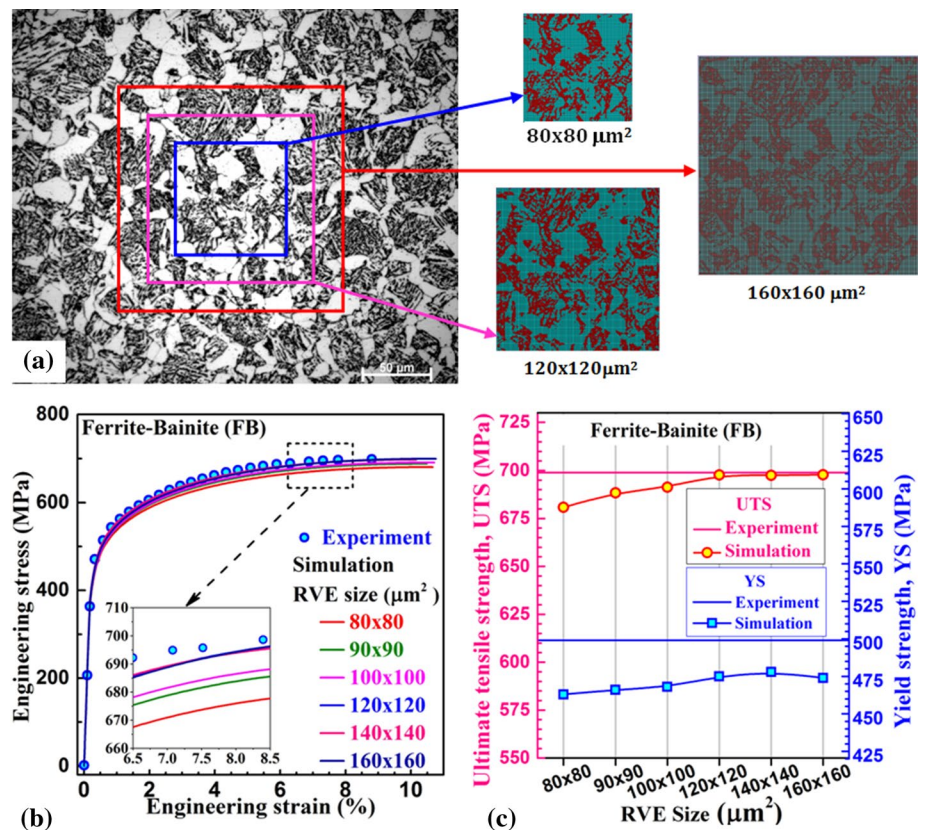
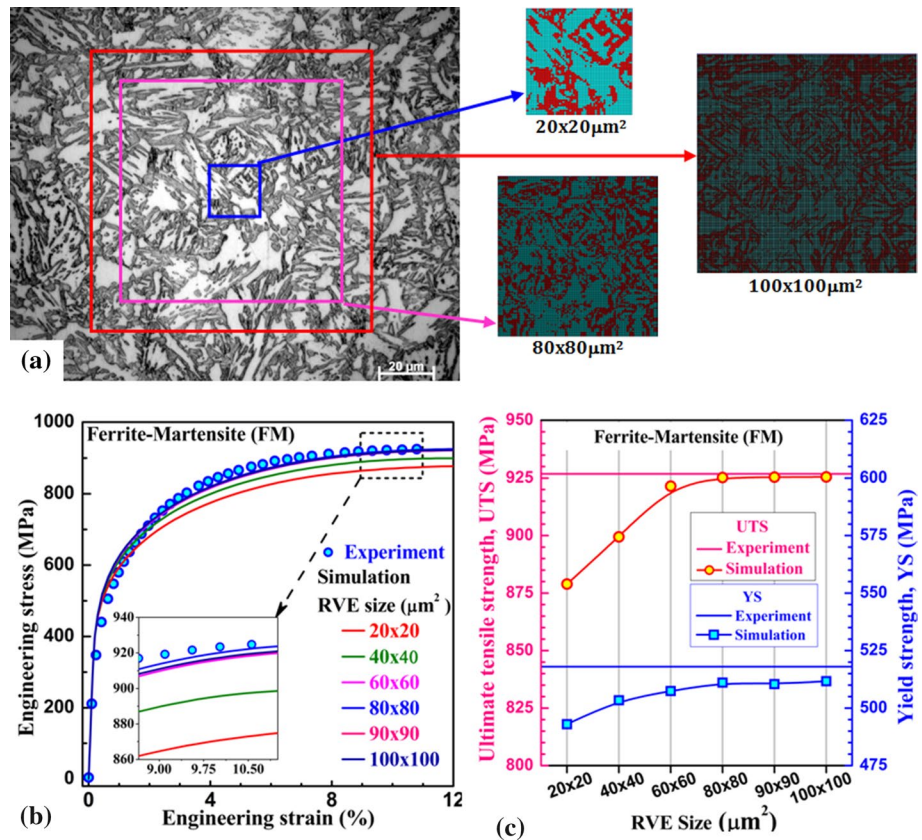


**Fig. 4 a** Selection of micro-structure based 2D RVE models from optical image of ferrite–martensite (FM) microstructure. **b** Effect of simulated stress–strain behaviour with variation in 2D RVE size. **c** Comparison of experimental yield strength as well as ultimate tensile strength with simulated results for varying RVE size



theory and incorporated in FE analysis as required input parameters.

### 3.2 Flow Behaviour of Microstructural Constituents

The FE analysis of multiphase steel requires the flow behaviour of its constituent phases to calculate the macroscopic response [34]. In the past decade, different methods were introduced for calculating the stress–strain behaviour of individual phases, like X-ray diffraction technique, dislocation based strain hardening model, analytical curve fitting, micro-pillar compression testing, nanoindentation [13, 35–37]. In this current work, individual phase flow behaviour was predicted using the dislocation based strain hardening model [13]. A correlation among true stress and true strain is expressed as:

$$\sigma_f = \sigma_0 + \Delta\sigma_c + \Delta\sigma \tag{1}$$

$\sigma_0$  is the peierls stress, which indicates the effect of chemical composition in solid solutions and can be expressed as:

$$\sigma_0 = 77 + 80\%Mn + 750\%P + 60\%Si + 80\%Cu + 45\%Ni + 60\%Cr + 11\%Mo + 5000\%N \tag{2}$$

$\Delta\sigma_c$  describes the strengthening due to interstitial carbon. For different phases like ferrite, martensite and bainite, the strengthening effect of interstitial carbon are different, and the value of  $\Delta\sigma_c$  is given as:

$$\Delta\sigma_c^f = 5000x(\%C_{ss}^f) \tag{3}$$

$$\Delta\sigma_c^m = 3065x(\%C_{ss}^m) - 161 \tag{4}$$

$$\Delta\sigma_c^b = 900x(\%C_{ss}^b) \tag{5}$$

where  $\%C_{ss}^f, \%C_{ss}^m$  and  $\%C_{ss}^b$  denotes the carbon weight percentage in ferrite, martensite and bainite phase respectively.

$\Delta\sigma$  describes the strengthening effects due to dislocation plus work softening caused by recovery, which can be expressed as:

$$\Delta\sigma = \alpha M \mu \sqrt{b} \sqrt{\frac{1 - \exp(-Mk_r \epsilon_p)}{k_r L}} \tag{6}$$

Considering the above three terms, the expression for calculating the flow curve for each phase is given by:

$$\sigma_f = \sigma_0 + \Delta\sigma_c + \alpha M \mu \sqrt{b} \sqrt{\frac{1 - \exp(-Mk_r \epsilon_p)}{k_r L}} \tag{7}$$

where,  $\sigma_f$  is the von Mises stress (true stress) and  $\epsilon_p$  is the equivalent plastic strain (true strain). The details about all parameters used in Eq. (6) are listed in Table 2.

**Table 2** Material parameters used to simulate flow behaviour of constituent phases

Parameters	Values
$M$ : Taylor factor	3
$b$ : Burgers vector	$2.5 \times 10^{-10}$ m
$\mu$ : Shear modulus	80,000 MPa
$\alpha$ : Constant	0.33 for Ferrite phase in Ferrite–pearlite 0.36 for Ferrite phase in ferrite–bainite 0.42 for Ferrite phase in ferrite–bainite 0.25 for pearlite in ferrite–pearlite 0.33 for bainite in ferrite–martensite 0.33 for martensite in ferrite–martensite
$k_r$ : Recovery rate	For ferrite: $10^{-5}/d\alpha$ , where $d\alpha$ is ferrite grain size For Bainite: $10^{-5}/d\gamma$ For martensite: 41
$L$ : Dislocation mean free path	For ferrite: $d\alpha$ For Bainite: $2 \times 10^{-7}$ m For martensite: $3.8 \times 10^{-8}$ m
$\lambda$ : Interlamellar spacing of pearlite	0.5 $\mu\text{m}$

The flow behaviour of soft ferrite phase depends on the microstructural parameters and also depends on the property of the second phase in different duplex microstructures. Hence the flow behaviour of the ferrite phase present in FP, FB and FM are different. It was investigated by performing the nanoindentation on the ferrite phase and comparing the load-penetration depth curve for the developed material. Hence the value of the constant parameter  $\alpha$  for the ferrite phase was calibrated from the nanoindentation load-depth curve and listed in Table 2.

Flow behavior of pearlite phase is primarily governed by the cementite lamellae. From the literature it was concluded that interlamellar spacing  $\lambda$  was the main microstructural parameter that controls the flow stress for pearlite phase [13]. Analogous to Eq. (6) the pearlite phase flow behaviour was estimated using the following expression:

$$\sigma_f = \sigma_0 + 3\mu b\lambda^{-1} + \alpha M\mu\sqrt{b} \sqrt{\frac{1 - \exp(-Mk_r\epsilon_p)}{k_r L}} \quad (8)$$

The values of all parameters considered to calculate the individual flow behaviour were taken from the earlier works [13, 38, 39] and are documented in Table 2. The percentage of carbon in ferrite phase was considered as the maximum solubility of carbon in ferrite phase that is 0.02 wt% and the carbon percentage in the second phase (i.e., pearlite, bainite and martensite) was calculated by applying the carbon mass balance equation [40].

## 4 Experimental Results and Discussion

### 4.1 Microstructure

Optical micrographs of differently heat treated steels have been presented in Fig. 1b–d. As expected, furnace cooling of the selected steel after austenitization (900 °C, 1 h) had developed a coarse polygonal ferrite plus pearlite microstructure (Fig. 1b). Image analyses of ferrite–pearlite microstructures were performed and the volume fractions of ferrite and pearlite were estimated as  $0.63 \pm 0.05$  and  $0.37 \pm 0.04$ , respectively. To develop ferrite–bainite microstructure, steel specimens after austenitization was directly transferred to salt bath for bainitic transformation (450 °C, 1 h); however, the volume fraction of bainite in the developed ferrite–bainite structure was found to be much higher ( $> 0.50$ ). Therefore, the heat treatment schedule for the ferrite–bainite treatment was slightly modified since the primary aim of the present study was to develop duplex microstructures with nearly same volume fractions of constituting phases but with different second phase/phase mixtures. In the modified ferrite–bainite treatment shown in Fig. 1a, steel specimens were kept in the two-phase region (ferrite + austenite) in between austenitization and bainitic treatment. This allowed part of the austenite to transfer into pro-eutectoid ferrite, and subsequent salt bath treatment resulted in the transformation of remaining austenite into bainite [41]. The developed ferrite–bainite microstructure is depicted in Fig. 1c. The estimated volume fraction of bainite was  $0.39 \pm 0.05$  which was nearly same to that of the pearlite content in the ferrite–pearlite structure. In addition, it can be seen that the shape, size and distribution of second phase constituent (i.e., pearlite and bainite) were very similar in the ferrite–pearlite and ferrite–bainite microstructures.

For ferrite–martensite microstructure, preliminary experiments revealed that direct intercritical annealing (725 °C, 1 h) of the as-received cold rolled steel or intercritical annealing after austenitization treatment generated banded ferrite–martensite dual-phase structure which was known to provide inferior ductility of dual-phase steel [42]. To avoid banded structure, cold rolled steels were subjected to normalising treatment and subsequently, normalised steel specimens were used for intercritical annealing followed by water quenching (Fig. 1a). This treatment developed martensite islands along the grain boundaries and triple points of polygonal ferrite (Fig. 1d) [43]. Furthermore, mean values of ferrite grain size were measured by image analyses method and found to be within  $20 \pm 4 \mu\text{m}$  when all three microstructures were considered. Therefore, it was inferred that the selected heat treatment schedules and associated parameters (Fig. 1a) help to develop three duplex microstructures having same matrix (ferrite) phase and nearly same volume fraction ( $0.37 \pm 0.03$ ) but different phase/phase mixtures, i.e., pearlite, bainite and martensite.

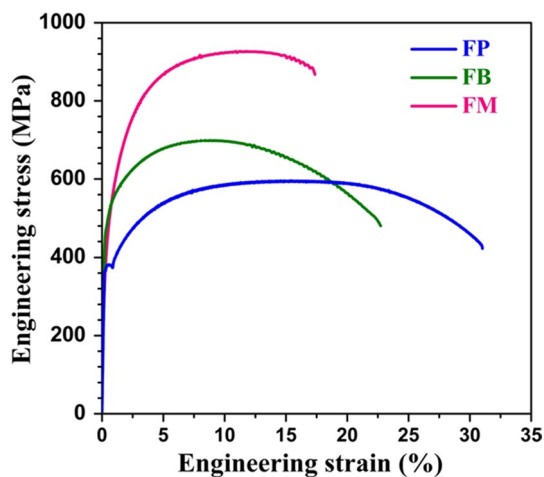


**Fig. 5** Engineering stress–strain curves of developed ferrite–pearlite (FP), ferrite–bainite (FB) and ferrite–martensite (FM) microstructures

## 4.2 Tensile Behaviour

The mechanical behaviour of all three developed duplex microstructures was examined by performing the tensile test of the materials till fracture. The engineering stress–strain graphs of ferrite–pearlite, ferrite–bainite and ferrite–martensite microstructures are presented in Fig. 5. It was observed that both ferrite–martensite and ferrite–bainite continuous yielding behaviour, unlike ferrite–pearlite one which showed a clear yield plateau region indicating non-uniform transition from elastic to plastic regimes. Continuous yielding in both ferrite–martensite and ferrite–bainite structures was attributed to the generation of mobile dislocations in the ferrite phase adjacent to the martensite or bainite at the time of austenite to martensite transformation during water quenching or austenite to bainite transformation at low temperature [44].

Tensile properties of different duplex structures are summarized in Table 3. Ferrite–pearlite structure had a very low yield and ultimate tensile strength but had higher uniform and total elongation values. On the other hand, ferrite–martensite structure yielded much higher strength with relatively lower ductility values (Table 3). Ferrite–bainite structure resulted in moderate yield strength and ultimate tensile strength as well as total elongation. It may be noted that amongst the three developed duplex microstructures, ferrite–bainite exhibited lowest uniform elongation but higher total elongation as compared to those of the ferrite–martensite; this was due to relatively higher non-uniform elongation of the former structure (Fig. 5).

Tensile fracture surfaces of the investigated microstructures are depicted in Fig. 6. Images in Fig. 6 revealed the presence of well-developed dimples of varying sizes indicating ductile mode of failure for both ferrite–pearlite (Fig. 6a1–a3) and ferrite–bainite (Fig. 6b1–b3) structures. On contrary, fractured surfaces of ferrite–martensite (Fig. 6c1–c3) exhibited dimples as well as cleavage facets suggesting mixed mode of fracture. Comparison of microstructure (Fig. 1d) and concerned fracture surfaces (Fig. 6c1–c3) suggested that the dimples were developed in the ferrite phase while cleavage facets corresponded to the hard martensite phase.

**Table 3** Summary of tensile properties of the investigated microstructures

Property	Ferrite–Pearlite	Ferrite–Bainite	Ferrite–Martensite
Yield strength (MPa)	378	499	518
Ultimate tensile strength (MPa)	596	699	928
Uniform elongation (%)	15.44	8.08	10.89
Total elongation (%)	31.04	22.73	17.36



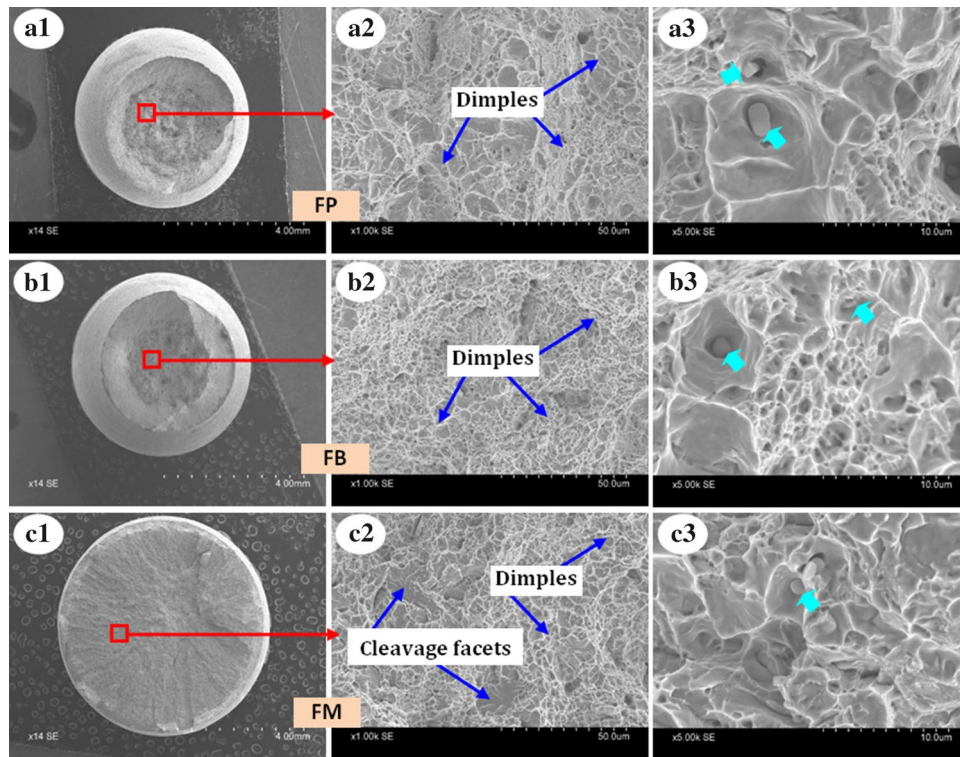


Fig. 6 SEM micrographs of tensile fracture surfaces at three different magnification for (a1–a3) ferrite–pearlite (FP), (b1–b3) ferrite–bainite (FB) and (c1–c3) ferrite–martensite (FM) structures

### 5 Simulation Results and Discussion

Finite element simulation with real microstructure based 2D RVE model was performed for three different duplex microstructural steels named as FP, FB and FM.

To establish a better correlation between macro–micro responses, the optimum size of the RVE model was derived by comparing the stress strain characteristics between simulation and experiment. The RVE model was constructed with axisymmetric element and boundary conditions

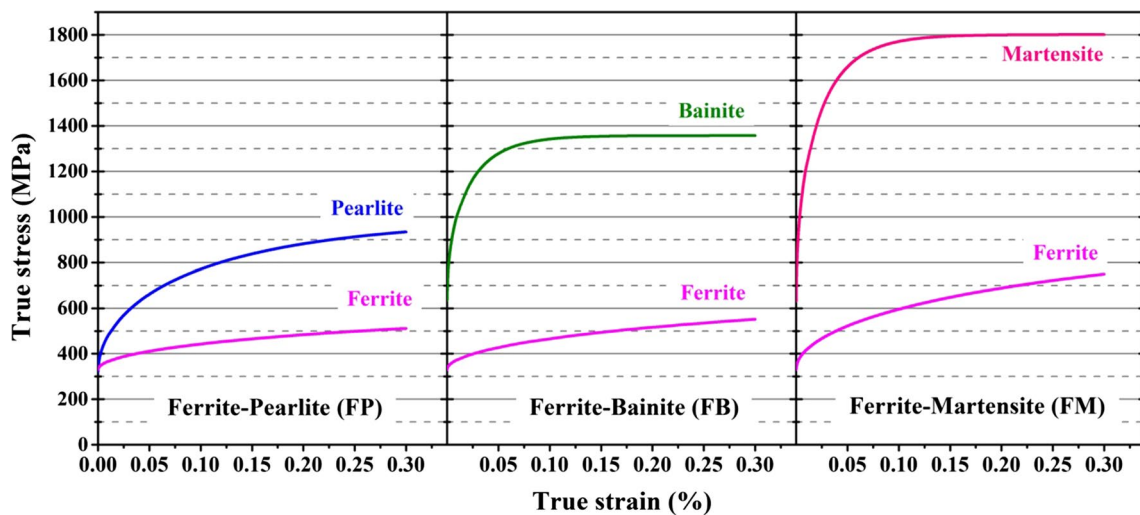


Fig. 7 Calculated flow behaviour of constituent phases in ferrite–pearlite (FP), ferrite–bainite (FB) and ferrite–martensite (FM) structures

and the ratio of radius and height of the RVE model was maintained during the iterations. The flow behaviour of individual phases were estimated using dislocation based formulation and illustrated in Fig. 7, which was incorporated in the FE simulation. The contour plot showed the variations in von Mises stress as well as equivalent plastic strain distribution of individual phases for three developed steels studied at different global strain levels to investigate their failure characteristics. The details of finite element simulations performed using RVE model is discussed in the following section.

### 5.1 Influence of Mesh Size

Influence of mesh size on finite element simulation response for prediction of flow behaviour or stress–strain distributions of multi-phase steels through constituent modelling approach led to a real challenge on the selection of the correct mesh sizes. Uthaisangsuk et al. [15] studied the influence of mesh densities on the strain and stress partitioning in the 2D RVE based simulation for DP-600 steel consisting of 0.27 volume fraction of martensite. It was inferred that mesh density of finer than  $260 \times 260$  elements did not alter the simulation result. Abid et al. [45] developed the microstructure based RVE model using Matlab code for Ferrite–martensite structure and used ABAQUS finite element platform to generate the meshed model with different element sizes. From the computational analyses, these authors observed that the stress–strain response was influenced by the mesh size. Also the predicted value of UTS and YS changed with the change in mesh size. Amirmaleki et al. [28] simulated the flow behaviour of DP500 using RVE model with mesh size varying from  $0.050 \mu\text{m}$  to  $0.075 \mu\text{m}$  and observed a small deviation in flow behaviour with change in the size of

the element. Therefore, in this present study, the real microstructure based RVE models of FM steel were constructed using mesh size varying from  $0.195 \mu\text{m}$  to  $0.52 \mu\text{m}$  with a constant increment of  $0.065 \mu\text{m}$ . The mesh sensitivity response for predicting the flow behaviour of FM steel is presented in Fig. 8. It can be noticed that there was a small variation in the prediction of flow behaviour with the mesh size variation from  $0.195$  to  $0.325 \mu\text{m}$ . However considerable variation in the prediction of flow behaviour when compared with the experiment was observed with the mesh size higher than  $0.325 \mu\text{m}$ . The close-up view of microstructure based meshed model of FM material with element size  $0.195 \mu\text{m}$  (fine mesh),  $0.325 \mu\text{m}$  and  $0.52 \mu\text{m}$  (coarse mesh) and their corresponding equivalent plastic strain distribution (PEEQ) are shown in Fig. 9. It was observed that the microstructural features were properly captured with fine mesh ( $0.195 \mu\text{m}$ ) and it continuously deteriorated with increase in mesh size. It was observed that the shear bands were more prominently visible from the simulation result considering finer mesh model compared to course mesh [46]. This was due to the increase in inaccuracy for capturing the morphology in the RVE model with the change in mesh size. This observation was very similar to the simulated response observed by [47], that with the reduction of element size, the simulation response generated a better correlation with the experimental results. Therefore the mesh size of  $0.325 \mu\text{m}$  was considered as the threshold value for subsequent calculation for all three structures. The maximum deviation of peak stress between experiment and simulation by FE model with mesh size  $0.325 \mu\text{m}$  was observed to be 0.3%. This mesh size was converged since further refinement of the element size to  $0.26 \mu\text{m}$  and  $0.195 \mu\text{m}$  lead to a change of 0.4% and 0.3% in the peak stress from the reference value respectively. Both the deviations were considered as negligible as the mesh was already converged.

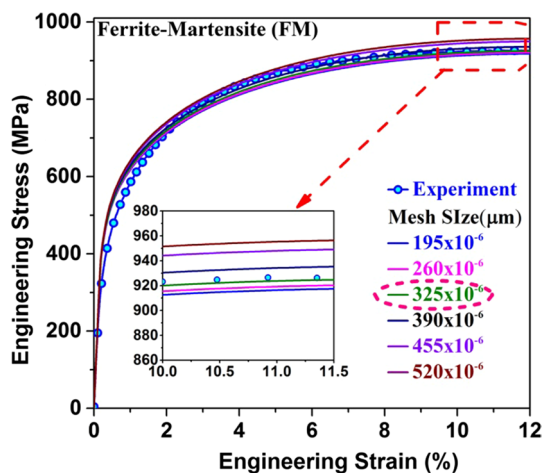


**Fig. 8** Comparison of experimental with simulated stress–strain behaviour considering microstructure based RVE model of ferrite–martensite (FM) steel for different mesh sizes

### 5.2 Influence of RVE Size

Micromechanics based finite element simulation of 2D RVE model for FP structure with 35% volume fraction of pearlite phase was performed to obtain the macroscopic response of the material. Optical microscopy image with 100X magnification was considered for generating the microstructure based RVE models for FP steel. Size of the RVE model was varied and the mesh convergence test was performed to estimate the appropriate dimension of RVE model. Similarly, the optical microscopy image for FB and FM structure were considered for generating their 2D RVEs. The volume fraction of hard phase and boundary condition remain unchanged in each case to perform the simulation. Figures 2b, 3b and 4b show the comparison between simulated stress–strain curve with the change in RVE sizes with the experimental results of FP, FB and

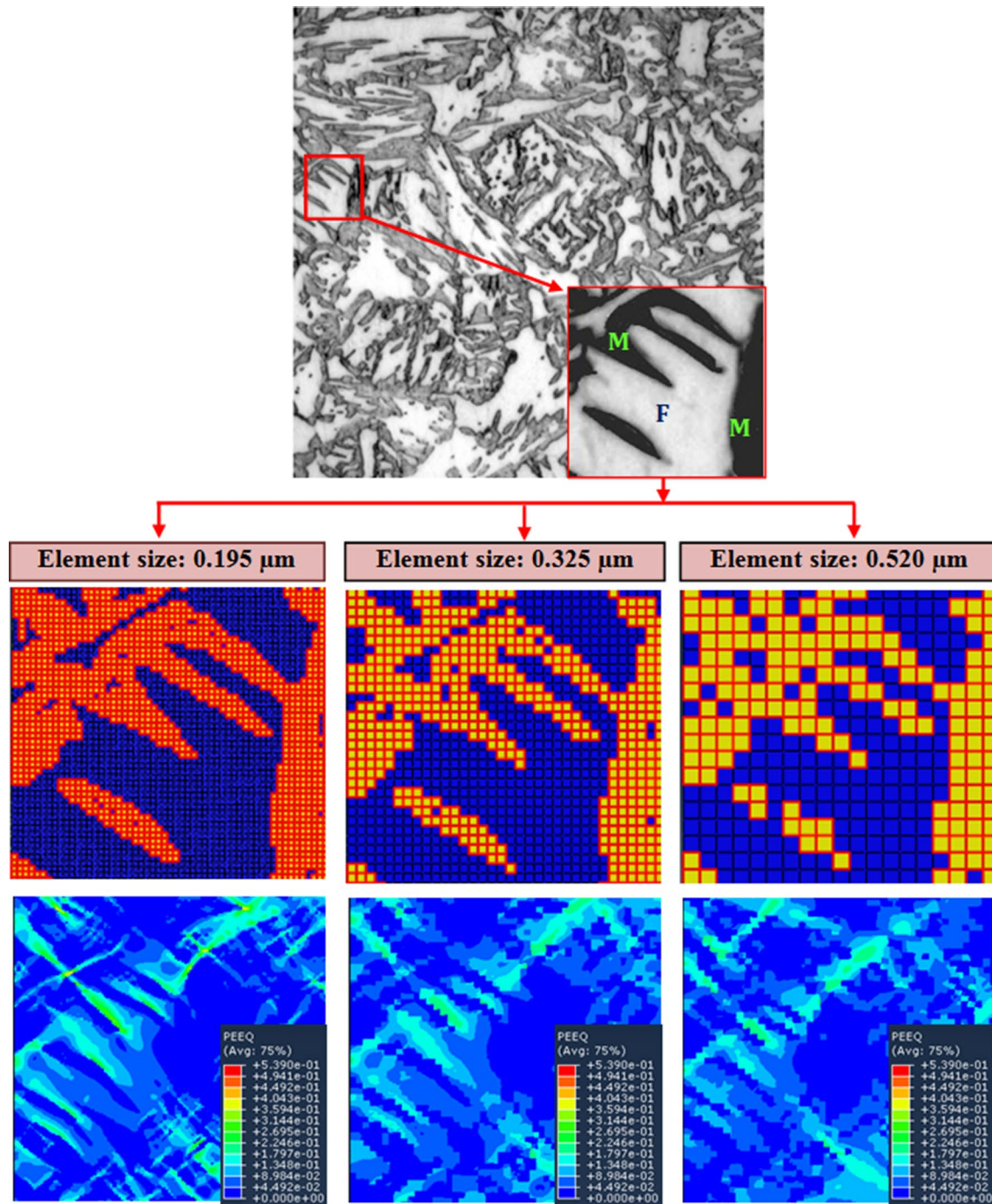


**Fig. 9** Illustrating the influence of mesh size on capturing the morphologies of constituting phases in RVE based modelling and consequently, on the distribution of equivalent plastic strain at global strain of 5.0% for ferrite–martensite (FM) structure

FM steels respectively. It was observed that the simulation response to predict the flow behaviour was enhanced with the increase in RVE size. When the RVE size was less than  $120 \mu\text{m} \times 120 \mu\text{m}$ , the simulated flow behaviour under predicted the experimental result whereas considering larger RVE size simulated stress–strain response was

well correlated with the experiment result of FP structure. Similarly, for FB the RVE size of  $120 \mu\text{m} \times 120 \mu\text{m}$  and of  $80 \mu\text{m} \times 80 \mu\text{m}$  for FM steel were demonstrated better responses. The ultimate tensile strength and yield strength predicted from the simulation with different RVE sizes were compared with the experimental result and they

were considered as the critical parameter for deriving the optimum size of the RVE model. The simulation response with RVEs larger than  $120\ \mu\text{m} \times 120\ \mu\text{m}$  in case of FP steel (Fig. 2c) and FB (Fig. 3c) steel and  $80\ \mu\text{m} \times 80\ \mu\text{m}$  for FM (Fig. 4c) steel demonstrated the convergence of the results. Therefore, the aforesaid RVE sizes were considered as the optimum size for the corresponding materials. A similar study was performed by Ramazani et al. [24] and found a minimum RVE size of  $24\ \mu\text{m} \times 24\ \mu\text{m}$  gives better simulation response for ferrite–martensite steel containing 35% martensite with two different martensite morphologies, i.e., banded martensite and equiaxial martensite structure.

### 5.3 Experimental Versus Predicted Flow Curves

A comparison between the flow behaviour obtained from the simulation response using optimum microstructure based RVE model observed in the present study as well as the virtually developed RVE model [14] and their experimental response for FP, FB and FM structures are presented in Fig. 10. Results in Fig. 10 revealed the simulation response with current RVE model for all three materials which showed a close correlation with the experimental response in comparison with virtually developed RVE model [14]. The computed ultimate tensile stress values for FP (Fig. 10a), FB (Fig. 10b) and FM (Fig. 10c) materials were 595.8 MPa, 699.82 MPa and 925.23 MPa against the experimentally observed values of 595.4 MPa, 699 MP and 928 MPa, respectively.

The contour plots of equivalent strain and von Mises stress distribution for FP, FB and FM structures at different global strains are presented in Fig. 11. It was observed that the hard phases (pearlite, bainite and martensite) significantly carried the higher stress in comparison to soft ferrite phase. On the contrary, the equivalent plastic strain predicted in soft ferrite phase was higher in comparison to hard second phase. Similarly, the difference in the intensity of von Mises stress as well as the equivalent plastic strain distribution was observed to be the highest in case of ferrite–martensite, intermediate for ferrite–bainite and the lowest for ferrite–pearlite structure. It was attributed to the variation in hardness level of constituent phases presented in different duplex microstructural steels. Earlier simulations performed on FM dual phase steels by Paul [16], Sun et al. [21], Marvi-Mashhadi et al. [23], Sodjit and Uthaisangsuk [30] and Choi et al. [48] also noticed a higher deformation level in ferrite phase in comparison with hard martensite phase which was in good agreement with the experimental finding by Azuma et al. [49].

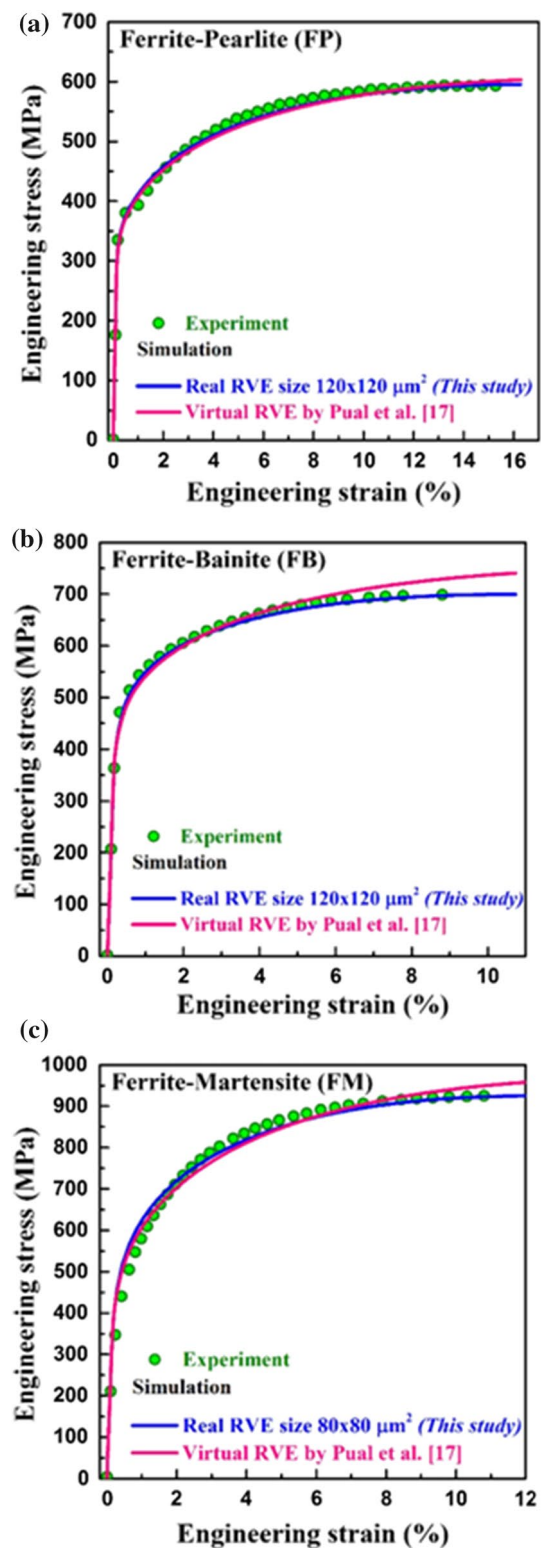


**Fig. 10** Comparison between experimental and simulated stress–strain behaviour with optimum RVE size for **a** ferrite–pearlite (FP), **b** ferrite–bainite (FB) and **c** ferrite–martensite (FM) structures

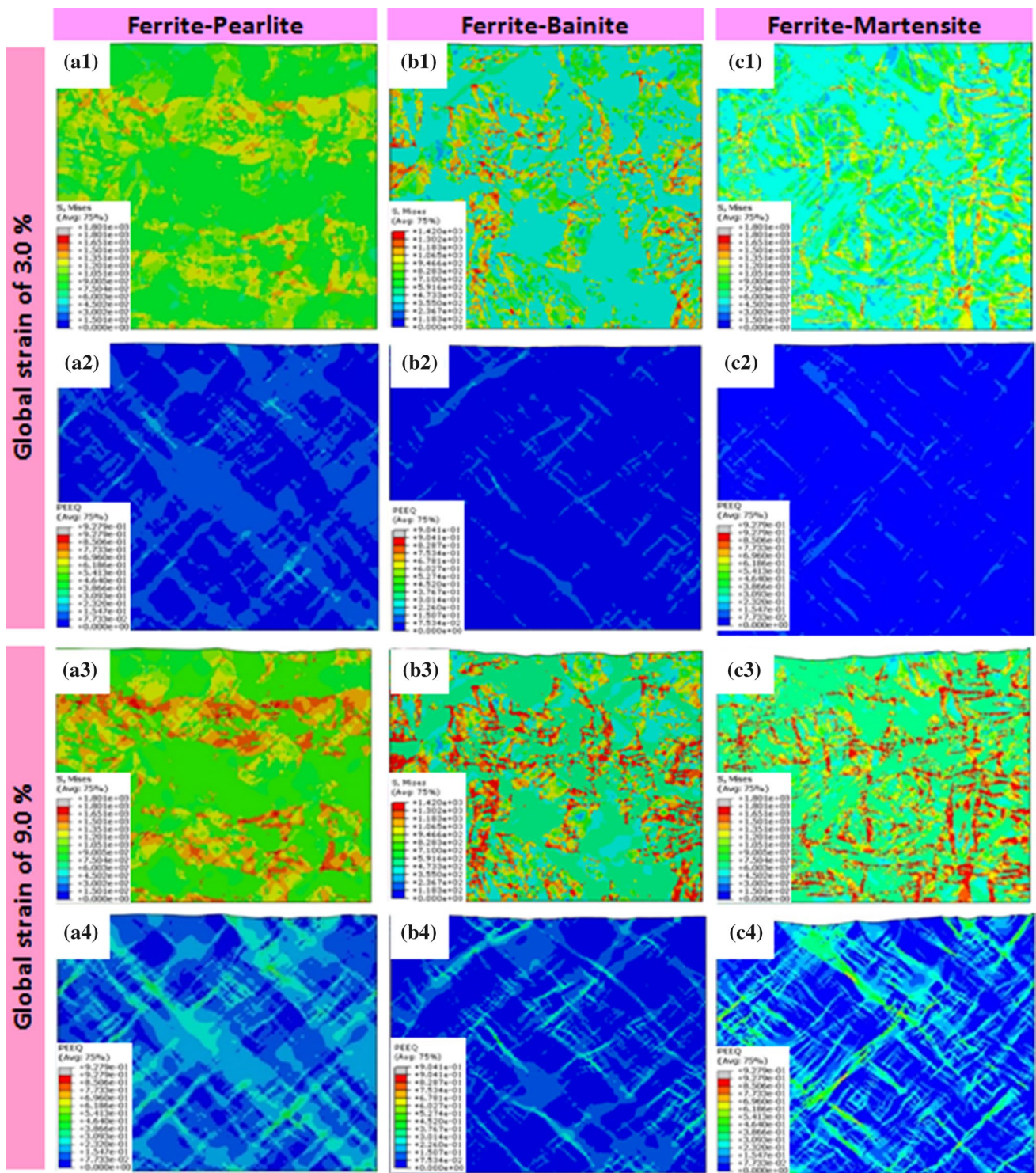
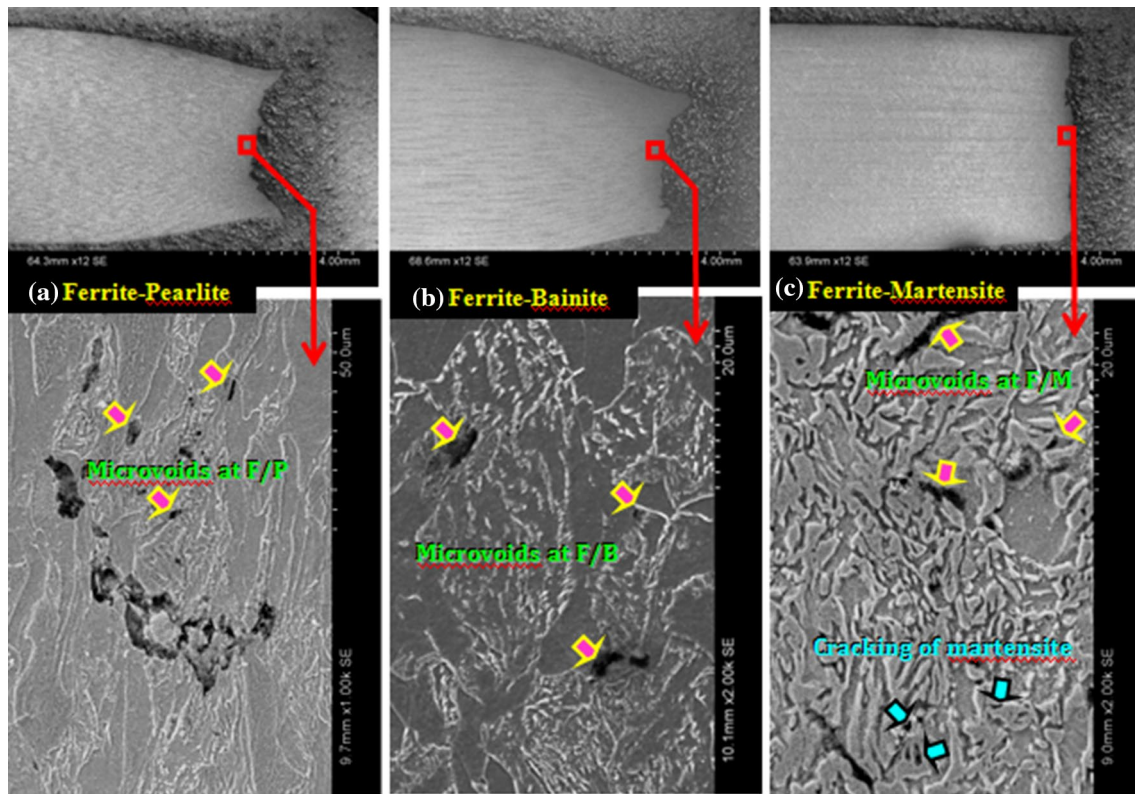


Fig. 11 von Mises stress distribution at global strain of 3.0% and 9.0% (a1, a3) for FP, (b1, b3) for FB, (c1, c3) for FM and equivalent plastic strain distribution at global strain of 3.0% and 9.0% (a2, a4) for FP, (b2, b4) for FB, (c2, c4) for FM structures



**Fig. 12** SEM micrographs of subsurface of fractured tensile specimens of **a** ferrite–pearlite, **b** ferrite–bainite and **c** ferrite–martensite structures exhibiting the locations of failure initiation

The SEM micrographs of the subsurface of the fractured tensile specimens close to the necking zone for FP, FB and FM steels are shown in Fig. 12. Micrographs in Fig. 12 indicated the presence of micro voids at the interfaces of soft (ferrite)-hard (pearlite/bainite) phases (arrow marks in Fig. 12) in both FP and FB steels as a result of the higher strain concentrations at this region. This observation has supported the results obtained from the simulation. These micro voids have become larger as a result of coalesce and further propagate along the softer ferrite phase which lead to the formation of necking before failure. The simulation response which captured the von Mises stress as well as the equivalent stress distribution at overall strain corresponding to ultimate tensile stress for FP and FB steel is demonstrated in Figs. 13 and 14, respectively. The contour plot for the same in its constituent phases clearly indicated the higher stress distribution in hard phases (pearlite/bainite) as compared to the softer phase. It can also be observed that the equivalent plastic strain is higher at the interface of

both the phases which lead to the formation of micro voids. On the other hand, fine or chain martensite structure was observed in case of the FM steel. The stress value on martensite is much higher compared to soft ferrite phase which lead to formation of voids in the narrow zone or junctions of martensite phases (arrow marks in Fig. 12). Figure 15 illustrates the distribution of von Mises stress and equivalent strain of FM steel and its constituent phases at global strain corresponding to ultimate tensile stress. It revealed the von Mises stress in martensite phase was much higher compared to the soft ferrite phase and a reverse trend was observed for plastic strain distribution. Besides, the formation of higher stress level due to the thin morphology of the martensite phase resulted in its cracking. The cracks occurred within the martensite phase served as nucleation sites for the micro void formation; this was observed from the microscopic analyses of the subsurface of fractured tensile specimen (Fig. 12).

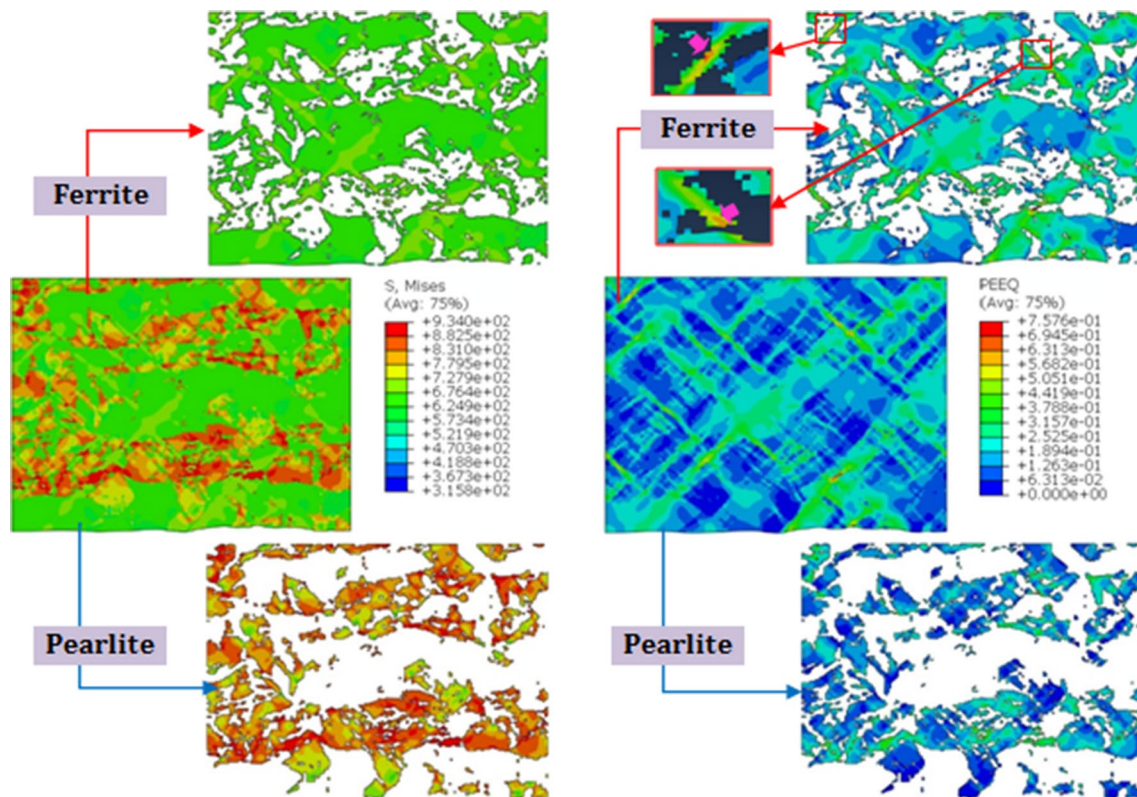


**Fig. 13** von Mises stress and equivalent plastic strain distribution in ferrite and pearlite at global strain corresponding to ultimate tensile stress

The observed results were further substantiated using the frequency distribution plot of the equivalent plastic strain distributions of constituent phases obtained from RVE simulation at different deformation levels to get a clear insight about the deformation behaviour of each phase. Results obtained from the frequency distribution for the constitutive phases are plotted in Fig. 16a. It indicates that, peak of the frequency distribution curve of the soft ferrite phase has been shifted towards the higher value of plastic strain and also becomes wider with an increase in the global strain. However, the corresponding plastic strain of the peaks of frequency distribution curves of bainite and martensite phases were found to be insignificant with increase in the global strain. It indicated that the deformation in major portion of bainite and martensite particles have not been affected much with variation in applied strain. The above observations can be attributed to the higher yield strength of both the bainite and martensite phases in comparison with the soft ferrite phase. But in

case of ferrite–pearlite steel, the variation of yield strength between ferrite and pearlite was much lower. Therefore, significant plastic strain observed in both the phases were responsible for producing higher value of uniform elongation as well as a distinct ductile failure of FP steel as compared to FB and FM steels.

The equivalent plastic strain distribution within the constituent phases was extensively explored by observing the variations of strain localisation factor (SLF) and average equivalent plastic strain in individual phases for the better prediction of the failure mode. The formulation mentioned in Zhao et al. [50] was used to estimate the SLF which is depicted in Fig. 16b as a function of applied strain. It was observed that with an increase in global strain, there was an increase in SLF for all three materials. The variations of SLF for FB and FM structures were quite similar; however, the same was observed to be comparatively lower in case of FP steel. The variations of average plastic strain as a function of global strain for constituent phases are shown in

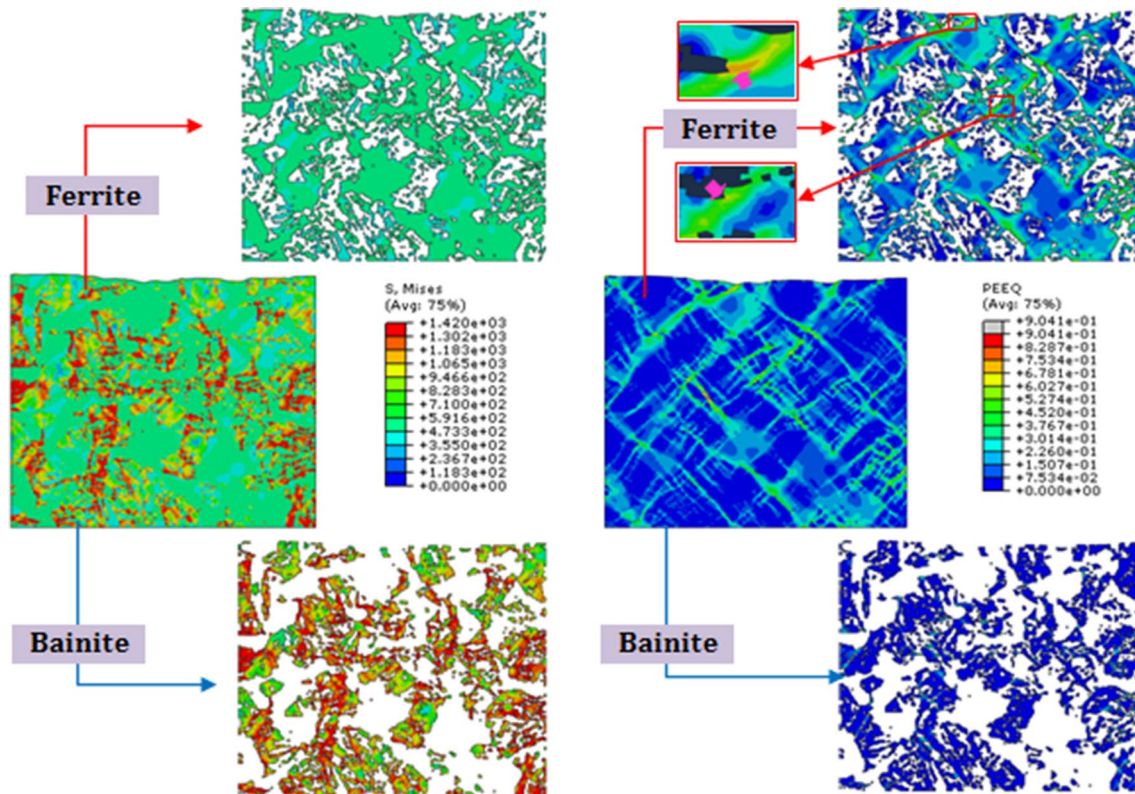


Fig. 14 von Mises stress and equivalent plastic strain distribution in ferrite and bainite at global strain corresponding to ultimate tensile stress

Fig. 16c. One can observe from Fig. 16c that the difference in the variation of equivalent plastic strain within the constituent phases of duplex microstructural steels was higher for  $FM > FB > FP$ . The lowest value observed in FP steel restricted the formation of stress concentration which possibly resulted in the higher elongation (Fig. 5). For FB and FM, a visible amount of stress concentration was, however, observed due to higher difference in the average plastic strain within its constituent phases which resulted in early failure of these materials.

## 6 Conclusions

In this study, deformation behaviour of three duplex microstructures; namely; ferrite–pearlite (FP), ferrite–bainite (FB) and ferrite–martensite (FM), with nearly same volume fraction of hard second phase/phase mixture was studied in detail by both experimentation and real microstructure based 2D RVE simulation. The obtained results and their pertinent analyses allowed to draw following major conclusions.

- The FP, FB and FM microstructures with nearly equal volume fraction ( $0.37 \pm 0.03$ ) of secondary hard phase (i.e., pearlite, bainite and martensite) were developed by means of a low carbon steel via the judicious selection of heat treatment schedules and associated parameters. In spite of nearly equal volume fraction of second phase or phase mixture, the FM structure provided superior strength and FP structure exhibited better elongation, while FB structure yielded moderate strength and ductility.
- Elasto-plastic finite element analysis was performed on the 2D representative volume element (RVE) models generated from real microstructures to predict the engineering stress–strain behaviour under uniaxial tensile loading. Accuracy of the simulated stress–strain response was strongly influenced by the element size. The optimized mesh size for the FM structure was found to be  $325 \times 10^{-6} \mu\text{m}$ ; the coarser mesh size overestimated the strength value while, the finer mesh size marginally



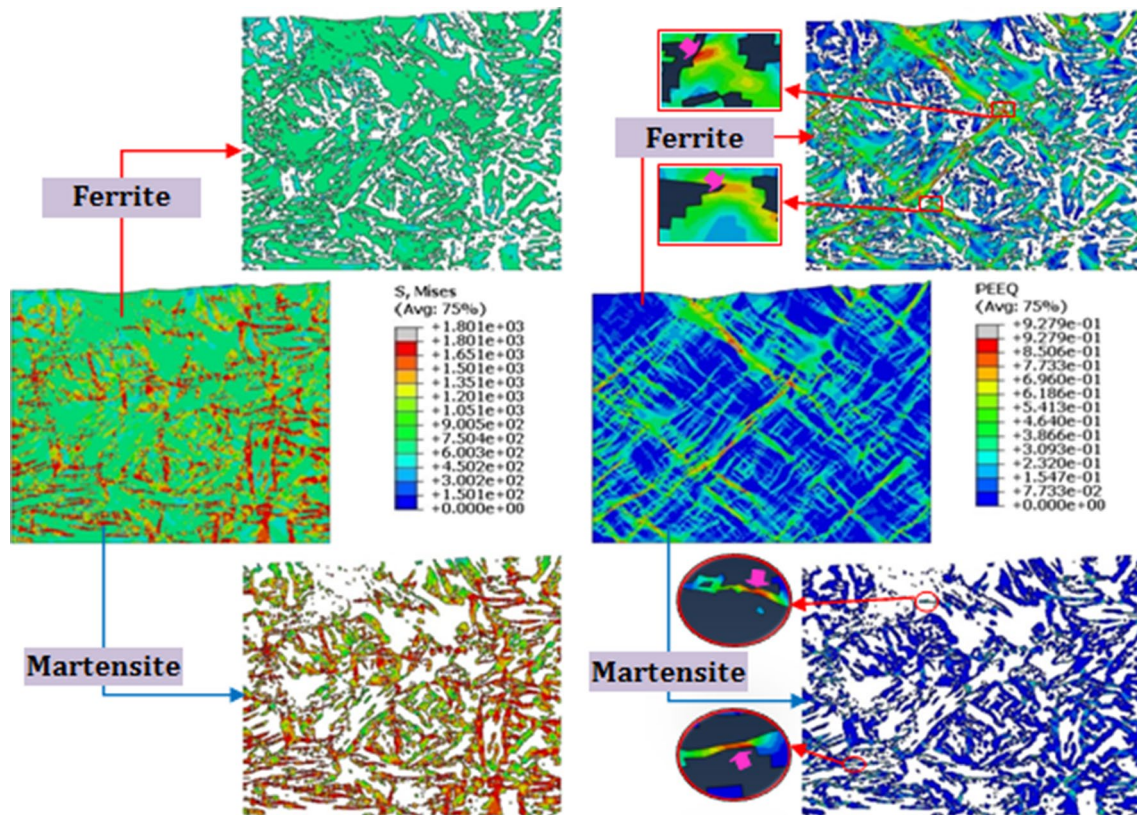


**Fig. 15** von Mises stress and equivalent plastic strain distribution in ferrite and martensite at global strain corresponding to ultimate tensile stress

underestimated the strength apart from taking higher computational time.

- The computed stress–strain behaviour varied considerably with the RVE size and the type of microstructure. For the convergence of experimental and simulated ultimate tensile strength values, the minimum RVE size was identified as  $80\ \mu\text{m} \times 80\ \mu\text{m}$  for FM, and  $120\ \mu\text{m} \times 120\ \mu\text{m}$  for both FP and FB structures. It was in conformity with the fact that the shape, size and distribution of second phase (pearlite and bainite) were nearly same in FP and FB structures; whereas, relatively fine and uniform distribution of second (martensite) phase reduced the requirement of minimum RVE size in case of FM structure.
- Strain distributions in the duplex structures varied significantly with the type of the second phase. For all

structures, soft ferrite matrix experienced much higher plastic strain as compared to hard second phase. As the strain increased gradually, the pearlite experienced higher plastic strain while bainite accommodated least strain. Strain localization in FB and FM was found to be nearly same in spite higher hardness of martensite over bainite. Strain localization in FP was considerably lower as compared to FM or FB that corroborated well with its higher ductility.

- Plastic strain distribution further revealed that strain was maximum at F–P and F–B interfaces while the same for FM was observed within the martensite particles apart from the F–M interfaces. These were well corroborated with the experimental observations of

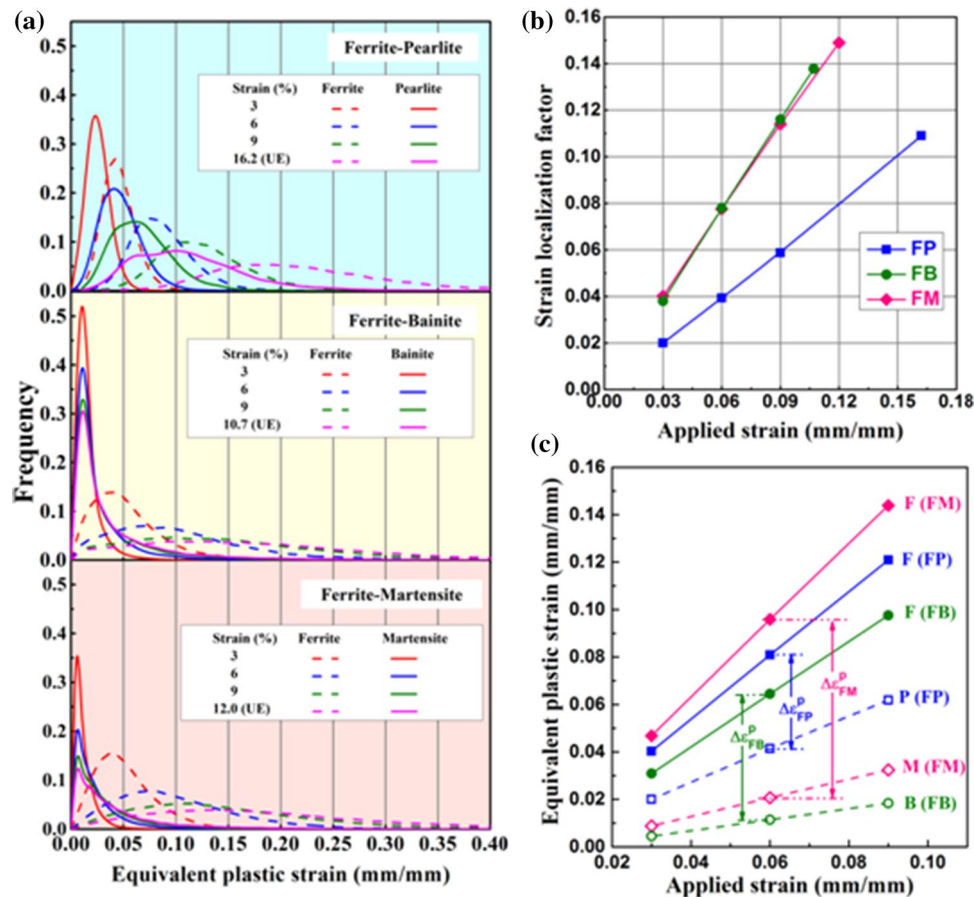


**Fig. 16** a Distribution of equivalent plastic strain of constituent phases for ferrite–pearlite, ferrite–bainite and ferrite–martensite steels at different simulated global strains; Influence of second phase/phase mixture on b strain localization factor and c equivalent plastic strain in constituting phases for all three i.e., ferrite–pearlite (FP), ferrite–bainite (FB) and ferrite–martensite (FM) structures. Note that the difference in plastic strain between the constituting phases varied widely with the types of microstructure. The difference in plastic strain between the constituting phases vary widely with the types of microstructure

void initiation at the interphase interfaces for all three duplex structures in addition to the cracking of the second phase, i.e., martensite in case of FM structure.

**Acknowledgements** The assistance received from the Centre of Excellence on Microstructurally Designed Advanced Materials Development, TEQIP-III of Indian Institute of Engineering Science and Technology (IIST), Shibpur to carry out a part of this work is gratefully acknowledged.

## References

- G.R. Speich, R.L. Miller, *Struct. Prop. Dual-Phase Steels* **1**, 424 (1979)
- M. Sarwar, R. Priestner, *J. Mater. Sci.* **31**, 2091 (1996)
- E. Ahmad, R. Priestner, *J. Mater. Eng. Perform.* **7**, 772 (1998)
- M. Habibi, R. Hashemi, E. Sadeghi, A. Fazaeli, A. Ghazanfari, H. Lashini, *J. Mater. Eng. Perform.* **25**, 382 (2016)
- G. Krauss, S.W. Thompson, *ISI J Int.* **35**, 937 (1995)
- T. Gladman, I.D. McIvor, F.B. Pickering, *J. Iron Steel Inst.* **210**, 916 (1970)
- C.M. Bae, C.S. Lee, W.J. Nam, *Mater. Sci. Technol.* **18**, 1317 (2003)
- S. Kumar, A. Kumar, Vinaya, R. Madhusudhan, R. Sah, S. Manjini, *J. Mater. Eng. Perform.* **28**, 3596 (2019)
- I.S. Kim, U. Reichel, W. Dahl, *Steel Res.* **58**, 186 (1987)
- A. Fallahi, *J. Mater. Sci. Technol.* **18**, 451 (2002)
- D.L. Bourell, A. Rizk, *Acta Metall.* **31**, 609 (1983)
- C.N. Lanzillotto, F.B. Pickering, *Met. Sci.* **16**, 371 (1982)
- R.-M. Rodriguez, I. Gutiérrez, *Mater. Sci. Forum* **426–432**, 4525 (2003)
- S.K. Paul, *Comput. Mater. Sci.* **56**, 34 (2012)
- V. Uthaisangasuk, U. Prahl, W. Bleck, *Eng. Fract. Mech.* **78**, 469 (2011)
- S.K. Paul, *Mater. Des.* **44**, 397 (2013)
- A. Fallahi Arezodar, A. Nikbakht, *J. Mater. Eng. Perform.* **28**, 53 (2019)
- F.M. Al-Abbasi, J.A. Nemes, *Int. J. Solids Struct.* **45**, 1449 (2003)

19. N. Ishikawa, D.M. Parks, S. Socrate, M. Kurihara, *ISIJ Int.* **40**, 1170 (2000)
20. B. Anbarlooie, H. Hosseini-Toudeshky, M. Hosseini, J. Kadkhodapour, *J. Mater. Eng. Perform.* **28**, 2903 (2019)
21. X. Sun, K.S. Choi, W.N. Liu, M.A. Khaleel, *Int. J. Plast* **25**, 1888 (2009)
22. S.A. Asgari, P.D. Hodgson, C. Yang, B.F. Rolfe, *Comput. Mater. Sci.* **45**, 860 (2009)
23. M. Marvi-Mashhadi, M. Mazinani, A. Rezaee-Bazzaz, *Comput. Mater. Sci.* **65**, 197 (2012)
24. A. Ramazani, K. Mukherjee, U. Prahl, W. Bleck, *Comput. Mater. Sci.* **52**, 46 (2012)
25. S.K. Basantia, V. Singh, A. Bhattacharya, N. Khutia, D. Das, *Mater. Today Proc.* **5**, 18275 (2018)
26. H.K.D.H. Bhadeshia, *Met. Sci.* **16**, 159 (1982)
27. ASTM, E8–99. “*Standard Test Methods for Tension Testing of Metallic Materials.*” *Annual Book of ASTM Standards. ASTM (2001).* (2001)
28. M. Amirmaleki, J. Samei, D.E. Green, I. van Riemsdijk, L. Stewart, *Mech. Mater.* **101**, 27 (2016)
29. F.M. Al-Abbasi, J.A. Nemes, *Comput. Mater. Sci.* **39**, 402 (2007)
30. S. Sodjit, V. Uthaisangsuk, *Mater. Des.* **41**, 370 (2012)
31. J. Zhou, A.M. Gokhale, A. Gurumurthy, S.P. Bhat, *Mater. Sci. Eng. A* **630**, 107 (2015)
32. K.S. Cheong, E.P. Busso, A. Arsenlis, *Int. J. Plast* **21**, 1797 (2005)
33. A. Ramazani, K. Mukherjee, H. Quade, U. Prahl, W. Bleck, *Mater. Sci. Eng. A* **560**, 129 (2013)
34. Y. Hou, T. Sapanathan, A. Dumon, P. Culière, M. Rachik, *Comput. Mater. Sci.* **123**, 188 (2016)
35. D.D. Tjahjanto, S. Turteltaub, A.S.J. Suiker, S. Van Der Zwaag, *Model. Simul. Mater. Sci. Eng.* **14**, 617 (2006)
36. N. Jia, Z.H. Cong, X. Sun, S. Cheng, Z.H. Nie, Y. Ren, P.K. Liaw, Y.D. Wang, *Acta Mater.* **57**, 3965 (2009)
37. H. Ghassemi-Armaki, R. Maaß, S.P. Bhat, S. Sriram, J.R. Greer, K.S. Kumar, *Acta Mater.* **62**, 197 (2014)
38. O. Bouaziz, P. B. Irsid, U. Group, G. Usinor, *Int. J. Metall.* **99**, 71 (2002)
39. P. Srithananan, P. Kaewtatip, V. Uthaisangsuk, *Mater. Sci. Eng. A* **667**, 61 (2016)
40. A. Ramazani, M. Abbasi, S. Kazemiabnavi, S. Schmauder, R. Larson, U. Prahl, *Mater. Sci. Eng. A* **660**, 181 (2016)
41. R. Bakhtiari, A. Ekrami, *Mater. Sci. Eng. A* **525**, 159 (2009)
42. M. Mazinani, W.J. Poole, *Metall. Mater. Trans. A Phys. Metall. Mater. Sci.* **38**, 328 (2007)
43. D. Das, P.P. Chattopadhyay, *J. Mater. Sci.* **44**, 2957 (2009)
44. P. Movahed, S. Kolahgar, S.P.H. Marashi, M. Pouranvari, N. Parvin, *Mater. Sci. Eng. A* **518**, 1 (2009)
45. N.H. Abid, R.K. Abu Al-Rub, A.N. Palazotto, *Comput. Mater. Sci.* **103**, 20 (2015)
46. L. Madej, J. Wang, K. Perzynski, P.D. Hodgson, *Comput. Mater. Sci.* **95**, 651 (2014)
47. H. Hosseini-Toudeshky, B. Anbarlooie, J. Kadkhodapour, G. Shadalooyi, *Mater. Sci. Eng. A* **600**, 108 (2014)
48. K.S. Choi, W.N. Liu, X. Sun, M.A. Khaleel, *Acta Mater.* **57**, 2592 (2009)
49. M. Azuma, S. Goutianos, N. Hansen, G. Winther, X. Huang, *Mater. Sci. Technol.* **28**, 1092 (2012)
50. Z.T. Zhao, X.S. Wang, G.Y. Qiao, S.Y. Zhang, B. Liao, F.R. Xiao, *Mater. Des.* **180**, 107870 (2019)

**Publisher’s Note** Springer Nature remains neutral with regard to jurisdictional claims in published maps and institutional affiliations.